

Molecular and Energetic Order Dominate the Photocurrent Generation Process in Organic Solar Cells with Small Energetic Offsets

Ke Zhou, Yanfeng Liu, Awwad Alotaibi, Jian Yuan, Chuanxiu Jiang, Jingming Xin, Xinfeng Liu, Brian A. Collins, Fengling Zhang, and Wei Ma*



Cite This: *ACS Energy Lett.* 2020, 5, 589–596



Read Online

ACCESS |



Metrics & More

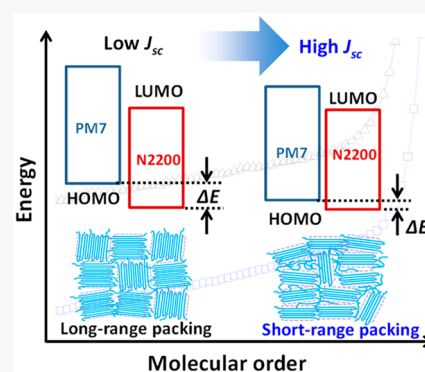


Article Recommendations



Supporting Information

ABSTRACT: Minimizing the energetic offset between the donor (D) and acceptor (A) in organic solar cells (OSCs) is pivotal for reducing the charge-transfer (CT) loss and improving the open-circuit voltage (V_{oc}). This nevertheless leads to a topic of debate regarding the driving force for the charge separation in OSCs with small energetic offsets. The molecular packing geometries in the active layer determine the energetic levels and trap density, but their relationship with the driving force is seldom considered. Limited by the complicated demixing morphology and inaccurate measurements of energy levels in the prototypical bulk-heterojunction (BHJ) devices, we thereby demonstrate a concise and robust planar-heterojunction model of PM7/N2200 to investigate the origin of driving force for charge generation. It is surprising to note that the device with smaller energy offset shows higher efficiency. Further analysis reveals that a bilayer device with short-range packing PM7 exhibits smaller energetic offsets along with fewer morphological defects and traps compared to its long-range packing counterparts. This molecular packing characteristic diminishes the energetic disorder at the D/A interfaces and inhibits the trap-assisted charge recombination, contributing to the increased short-circuit current (J_{sc}) and V_{oc} . Our results suggest that the energetic offset actually has limited influence on charge separation, while the synergetic control of molecular and energetic order is vital to the photocurrent generation and energy loss reduction in OSCs.



Organic solar cells (OSCs) have exhibited continuous development during recent years in various areas. The power conversion efficiency (PCE) has reached 16% in the single-junction and >17% in the tandem geometry,^{1–3} while devices with large-area active layers also exhibit rather impressive efficiency either on rigid or flexible substrates.^{4,5} In addition, OSCs feature obvious potential for manufacture toward versatile applications, such as indoor and semitransparent devices.^{6,7} Inspired by their long-term device stability under different external stresses, OSCs show a bright future in large-scale production and practical applications.^{8–10}

Compared to their inorganic counterparts, OSCs still present relatively large energy loss during the charge generation and transport process, limiting the improvement of open-circuit voltage (V_{oc}) and device efficiency.^{11–13} Many efforts have been made to reveal the underlying mechanism for the large energy loss in OSCs, and the intrinsic reason was found to be the formation of the charge-transfer (CT) state at the donor/acceptor (D/A) interfaces during the charge separation process due to the high binding energy of photoinduced excitons in organic semiconductors.^{14,15} This

produces two kinds of energy loss pathways in principle, namely, charge transfer loss ($E_g - E_{ct}$) and charge recombination loss ($E_{ct} - qV_{oc}$).¹⁸ Under this scenario, reducing the energy loss raised by the charge generation process is an important strategy to improve device V_{oc} .

Employing D/A combinations with small highest occupied molecular orbital (HOMO) or lowest unoccupied molecular orbital (LUMO) energetic offsets is the typical approach to minimize the value of $E_g - E_{ct}$. Indeed, the necessity of energetic offset for the efficient charge generation in OSCs is still a disputable topic. Tajima et al.¹⁷ found that the threshold energy difference from 0.2 to 0.3 eV was requisite for the charge generation process, while Nelson et al.¹⁸ also demonstrated that the CT state dissociation was efficient only in the high-energy offset blend by comparing different D/

Received: January 5, 2020

Accepted: January 23, 2020

Published: January 23, 2020

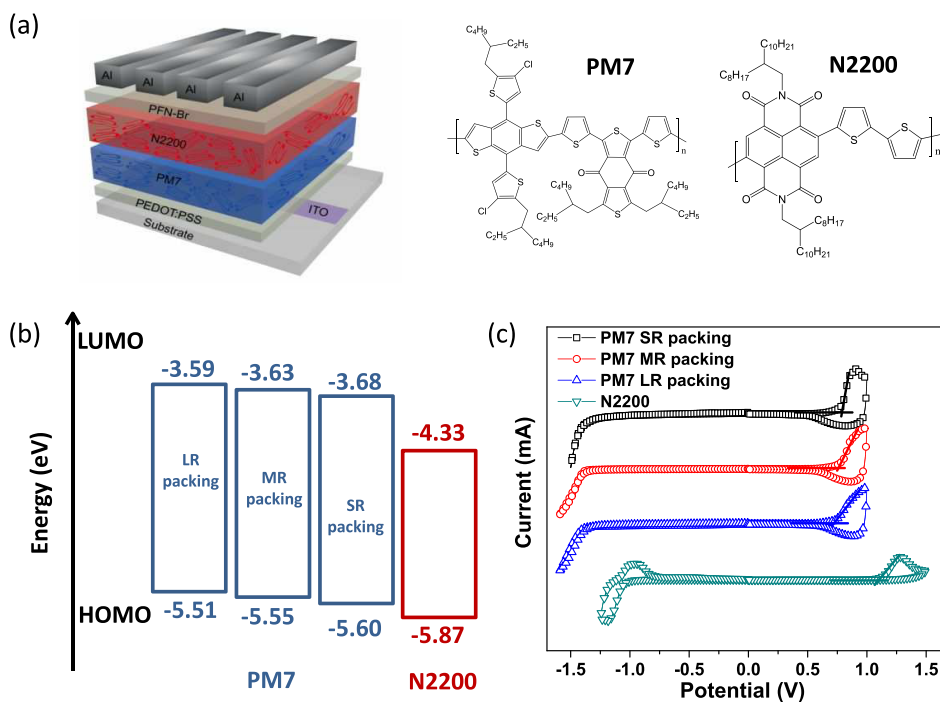


Figure 1. (a) Device geometry and chemical structure of PM7 and N2200 used in this study; (b) energy levels of donor with different molecular packing and acceptor; (c) cyclic voltammetry (CV) curves of donor with different molecular packing and acceptor.

A blend systems. On the other hand, Gao et al.¹⁹ proposed that a low energy offset between donor and acceptor molecular states could ensure not only the low energy loss but also efficient photocurrent generation process. More interestingly, Yan et al.²⁰ found that an excellent device efficiency of >10% could be achieved in a D/A blend with both negligible HOMO and LUMO energetic offsets. The large molecular electrostatic potential between donor and acceptor, which could induce intermolecular electric field, should be one possible reason for the efficient charge generation process in the blend with small energetic offset.^{21,22} Besides, Friend et al.²³ concluded that small Urbach energy could also promote free charge separation by outcompeting the nonradiative recombination of the CT state.

The inconsistent conclusions from different aspects might be due to the ignored factor of active layer morphology. In addition to the views of molecular potential and energy, interfacial morphologies associated with the charge generation and separation processes are nevertheless seldom studied in the systems with small energetic offsets. The active layer morphology is believed to be the original and crucial factor determining the device performance because of its fundamental influence on the D/A energy levels and trap density. The lack of the morphological analysis, on the other hand, probably aggravates the contradiction in the role of energetic offsets on the charge generation process in those different bulk-heterojunction (BHJ) systems. However, in the prototypical BHJ devices, energy level measurements of the donor and acceptor are considerably difficult because of their mixing and aggregation behaviors, hindering the accurate identification of energetic offsets in the BHJ.²⁴ Besides, the coupling process of crystallization and demixing between donor and acceptor provides the possibility of constructing a complicated morphology with randomly distributed domain size, mixing phase, and molecular packing.²⁵ These inevitably limit the simultaneous photocurrent improvement and energy loss

reduction in terms of morphological optimization. All-polymer solar cells have great potential to achieve high V_{oc} accompanied by favorable morphology stability and high blend ratio tolerance;²⁶ revealing the driving force–morphology relationship in those systems will probably further improve the device efficiency and promote OSC development.

Here, we employed the PM7/N2200 planar heterojunction model (polymer chemical structures can be found in Figure 1a) to study the driving force for the photocurrent generation process in terms of molecular packing. The HOMO levels of PM7 layers were gradually upshifted with the extended range of the molecular packing upon thermal annealing (TA) at different temperatures. Then, bilayer devices were prepared with a one-step-transfer method by adhering N2200 layers onto the PM7/PEDOT:PSS/ITO layers with different molecular packing. Interestingly, the photocurrent of the bilayer device with small energetic offset was unexpectedly larger compared to its counterparts with increased energetic offset. After analyzing the sensitive external quantum efficiency (EQE) results, we found that the energetic disorder (Urbach energy) decreased in the short-range packing device, which readily facilitated the charge separation process. In addition, trap-assisted charge recombination could reduce as well in the short-range packing device. Combined with the grazing-incidence wide-angle X-ray scattering (GIWAXS) results, we inferred that the possible reason was that the PM7 short-range packing film exhibited fewer morphological defects, which featured both adequate amorphous regions and minimal crystal boundaries compared to its long-range packing counterpart. This work suggests that synergetic control of molecular and energetic order, rather than energetic offset, is vital to the photocurrent generation process, which paves the way to achieving efficient OSCs with small energy loss.

The energetic levels of PM7 neat films could be easily adjusted by changing their molecular packing upon TA at different temperatures (as-cast and 140 and 200 °C). As shown

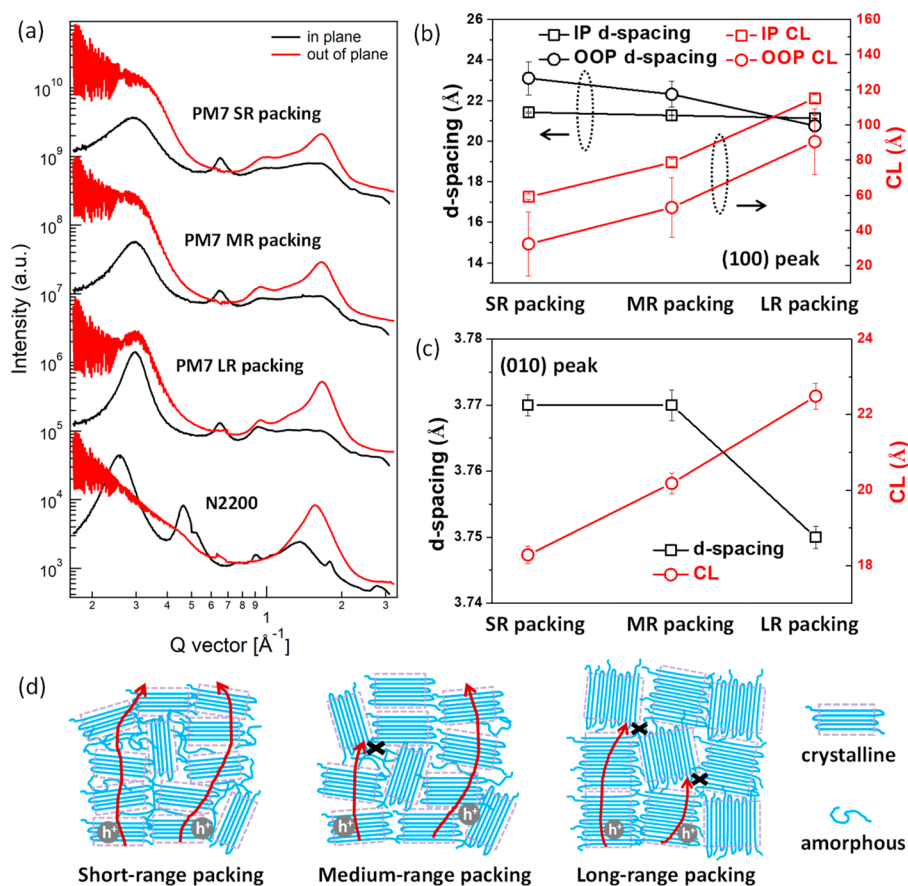


Figure 2. (a) GIWAXS measurement of PM7 films with different molecular packing and N2200 film. Corresponding d -spacing and coherence length of (b) (100) and (c) (010) peaks fitted based on the GIWAXS profiles for PM7 films with different molecular packing. The trend lines in panels b and c are guides-to-the-eye. (d) Illustration of PM7 films with short-range, medium-range, and long-range packing from left to right. The red arrows denote the possible hole transport pathways, and the black intersections denote the potential traps for the hole transport in the PM7 films.

in Figure 1b, with the PM7 molecular packing changing from short-range (SR) to medium range (MR) and long-range (LR), their HOMO levels gradually upshifted from -5.60 to -5.55 and -5.51 eV, which were measured by cyclic voltammetry (CV) (Figure 1c). In addition, we found the HOMO level of the N2200 film was -5.87 eV, which is close to the SR packing PM7 film. The ultraviolet photoelectron spectroscopy (UPS) was also used to measure the HOMO levels of polymers, and the results are shown in Figure S1, which exhibits a trend similar to that of CV results. The optical bandgap (E_g) of each polymer was obtained based on the intersection of the UV absorption and photoluminescence spectra (Figure S2).^{14,19} Therefore, the cascade energetic offsets of HOMO levels at D/A interfaces were constructed by making the bilayer devices. This provides a favorable model to study the effect of energetic offset on the charge generation process. To further confirm the different energetic offsets resulting from the various molecular packing, the values of $E_g - E_{ct}$ were calculated based on identifying the low-bandgap component and the fitted energy of CT states (Figure S3 and Table S1). With the increased molecular packing range, the values of $E_g - E_{ct}$ were gradually improved from 0.02 to 0.04 and 0.16 eV. We note that those values deviate from the results obtained with CV and UPS, which is possibly due to the regime difference and can be found in other work as well.^{27,28} However, the trend is in good agreement with the CV and UPS measurements.

The detailed molecular packing information was studied by the GIWAXS. As shown in Figures 2a and S4, all the PM7 films show obvious (100) diffraction peaks at $q = 0.29 \text{ \AA}^{-1}$ and (010) diffraction peaks at $q = 1.67 \text{ \AA}^{-1}$ in both the in-plane (IP) and out-of-plane (OOP) directions, suggesting the coexistence of face-on and edge-on orientation for PM7 molecules. The N2200 film exhibits preferential face-on orientation, as evidenced by the appearance of the (100) diffraction peak at $q = 0.26 \text{ \AA}^{-1}$ and (010) diffraction peak at $q = 1.57 \text{ \AA}^{-1}$ in the IP and OOP directions, respectively. We also studied the molecular packing in PM7/N2200 bilayer films, which exhibit a trend similar to that of their corresponding neat films (Figure S5). Figure 2b and Table S2 show the fitted PM7 molecular packing information based on the GIWAXS profiles. The d -spacing values decrease slightly from 21.42 to 21.27 and 21.13 \AA for the IP (100) diffraction peaks with the molecular packing from short-range to long-range, while the OOP (100) diffraction peaks also follow the variations. More obviously, the coherence length (CL) values^{29,30} increase from 59.06 to 78.68 and 115.14 \AA for the IP (100) diffraction peaks, while those values also improve from 32.28 to 53.01 and 90.47 \AA for the OOP (100) diffraction peaks. In addition, the OOP (010) diffraction peaks exhibit the similar trend as well (Figure 2c). We also measured the absorption spectra of PM7 films (Figure S6), the increased peak intensity from 0–0 transition at 620 nm becomes more pronounced in the long-range packing film, suggesting a more ordered molecular packing.

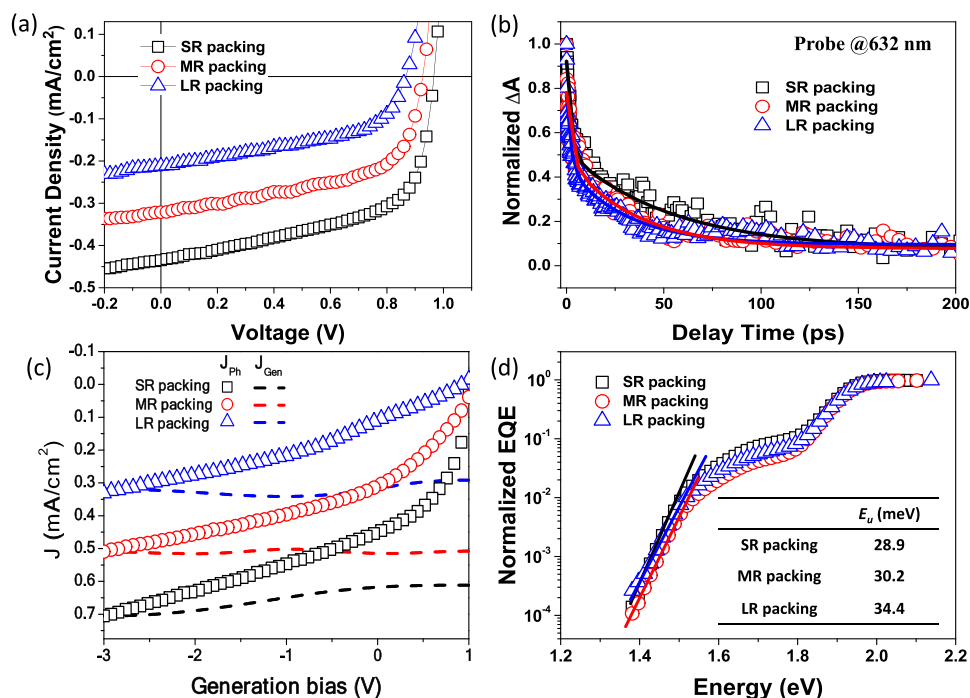


Figure 3. (a) I – V curves, (b) decay curves probed at 632 nm based on the TAS, (c) voltage dependence of the J_{ph} and J_{Gen} extracted as probed by TDCF experiments, and (d) normalized sensitive external quantum efficiency (EQE) of bilayer devices with different PM7 molecular packing. The table shows the E_u values by fitting the absorption edge of the EQE.

Table 1. Photovoltaic Parameters of Different PM7/N2200 Bilayer Devices

acceptor	donor	V_{oc} (V) ^a	J_{sc} (mA/cm ²)	FF (%)	PCE (%)
N2200	PM7-SR packing	0.96 ± 0.01	0.42 ± 0.04	59.4 ± 1.6	0.24 ± 0.03
	PM7-MR packing	0.92 ± 0.01	0.31 ± 0.03	56.1 ± 1.6	0.16 ± 0.02
	PM7-LR packing	0.87 ± 0.01	0.22 ± 0.02	50.0 ± 1.7	0.09 ± 0.01

^aThe average numbers and errors were obtained based on 10 devices.

Those are the reasons we designate PM7 films upon TA at different temperatures as short-range, medium-range, and long-range packing. Considering the analysis above, we illustrate the molecular packing in different PM7 films in Figure 2d. With the increased CL values in both the face-on and edge-on orientations, the amorphous regions distributing between adjacent crystal domains diminish gradually. Meanwhile, the extended molecular order in different orientations inevitably creates plenty of crystal boundaries. Both of them probably influence the charge separation and transport by forming morphological defects and traps. Recently, Lai et al.³¹ found that the π -interconnection (sporadic packing) rather than the π -order of conjugated polymer can effectively promote charge transport, which could support our hypothesis favorably. Therefore, it is desirable to uncover the effect of molecular packing on the photoelectric conversion process in the PM7/N2200 bilayer devices.

The I – V curves of bilayer devices with different molecular packing were measured, and the results are shown in Figure 3a and Table 1. The value of V_{oc} was 0.96 V in the SR packing device, while this value continuously reduced to 0.87 V in the LR packing device. The energy losses of those devices were studied based on the Rau model, in which three parts of charge losses can be identified, namely, charge-transfer loss (ΔE_1 , $E_g - E_{ct}$), radiative recombination loss (ΔE_2) and, nonradiative recombination loss (ΔE_3).^{14,15} As shown in Figure S7 and Table S3, the values of ΔE_1 increased gradually from 0.02 to

0.04 and 0.16 eV with the extended molecular packing, while the values of ($\Delta E_2 + \Delta E_3$) showed an irregular trend, changing from 0.56 to 0.58 and 0.51 eV. This indicates that energy loss resulting from charge generation is mainly responsible for the V_{oc} variation, and lowering the energetic offsets between donor and acceptor is crucial to realize high V_{oc} . On the other hand, the values of short-circuit current (J_{sc}) also decreased from 0.42 to 0.31 and 0.22 mA/cm² with the extended molecular packing, and the variation is further confirmed by the EQE measurements (Figure S8). This is somewhat contradictory with previous observation that a proper energetic offset will promote charge separation.^{32–34} In order to exclude the effect of TA on the morphological change at the interface between the PM7 and PEDOT:PSS layers, the bilayer devices were additionally prepared by a two-step transfer method, in which the preannealed PM7 layer was adhered onto the PEDOT:PSS layer first and then the N2200 layer was put onto the PM7 layer (Scheme S1). We found that the efficiency variations in the SR and LR packing devices were similar to their previous counterparts manufactured with a one-step transfer method (Figure S9 and Table S4). In addition, the surface morphologies of PM7 layers with different molecular packing were also examined with atomic force microscopy (AFM). All the films present similar morphology and comparable root-mean-square (RMS) roughness values of 1.60, 1.65, and 1.45 nm (Figure S10). Those suggest that the roughness of interfaces for the PEDOT:PSS/PM7 and PM7/N2200 layers

upon TA has negligible effect on the performance difference. Therefore, the molecular packing of the PM7 layer exclusively dominates the photoelectric conversion process. We thereby explore the fundamental mechanism on the SR-packing-induced better photocurrent for the PM7/N2200 device in terms of charge generation and the recombination process.

Transient absorption spectroscopy (TAS) measurements were performed to study the charge dynamics in the bilayer films. The ground-state bleaching (GSB) signals appear in the range of 500–660 nm and 580–766 nm for the neat PM7 and N2200 films (Figure S11), respectively. For all the bilayer films, those GSB signals overlap and exhibit two peaks at 632 and 703 nm. However, because of the limited detecting range, the photoinduced absorption (PIA) signal cannot be observed. Thus, the GSB signals at 632 nm in the bilayer devices were fitted to deriving the exciton dynamics produced in the PM7 layers. As shown in Figure 3b and Table S5, the comparable delay time (τ_1) at ~ 2 ps arises in all the bilayer films, while the longer delay time (τ_2) appears in the range of 30–60 ps. We calculated the average delay time (τ_{ave}) and found that it decreased from 51.8 to 33.5 and 29.0 ps with the extended molecular packing, revealing a longer lifetime of singlet excitons in the SR packing bilayer film.^{35,36} This can be potentially ascribed to the fewer morphological defects in the SR packing film and would readily promote the exciton diffusion toward the D/A interfaces.

In order to study the charge generation process, the time-delayed collection field (TDCF) measurements for all the bilayer devices were conducted. TDCF is an optical pump and electronic probe experiment. By setting the delay time, the generation current (J_{Gen}) can be obtained based on the different lifetime of CT states (~ 1 ns) and free charges (~ 2 μs).^{37,38} As shown in Figure 3c, the J_{Gen} is independent of applied electric field in the studied devices, while it increases apparently from 0.30 to 0.51 and 0.61 mA/cm^2 with the reduced molecular packing. This suggests that charge separation and extraction in the SR packing device is relatively efficient, which contributes to the higher J_{Gen} value. Besides, the $J_{\text{ph}}-V_{\text{eff}}$ curves in the bilayer devices with different molecular packing were also measured and the shapes of all the $J_{\text{ph}}-V_{\text{eff}}$ curves exhibit the characteristic of applied voltage-dependent photocurrent (Figure S12). In the device with LR packing, the slope of the curve at the high voltage range is obviously larger than those of their SR and MR packing counterparts. Typically, the external applied voltage could assist the dissociation of photogenerated excitons at the D/A interfaces, and the large slope of $J_{\text{ph}}-V_{\text{eff}}$ curve implies a more difficult process associated with charge separation.³⁹ Moreover, the origin of different charge generation was further explored based on the sensitive EQE measurements. Urbath energy (E_u), which is related to energetic disorder, can predict the ease of the charge separation process. A high value of E_u indicates the expanding possibility for exciton trapping in the tail of CT states and thus is detrimental to the charge separation process. Usually the E_u value of the photovoltaic device can be inferred by fitting the sensitive EQE curves and then calculated by using eq 1:^{40,41}

$$\text{EQE}(E) \propto \alpha(E) \propto \exp\left(\frac{E}{E_u}\right) \quad (1)$$

where α is the absorption coefficient and E is the incident photon energy. As shown in Figure 3d, the calculated E_u values

are 28.9, 30.2, and 34.4 meV for the SR packing, MR packing, and LR packing devices, respectively, which favorably explains the superior charge separation process in the SR packing device.

Charge recombination is another key factor determining the photocurrent generation process and thus is investigated in those bilayer devices. The light intensity-dependent V_{oc} was first performed, and the results are shown in Figure 4a. As is

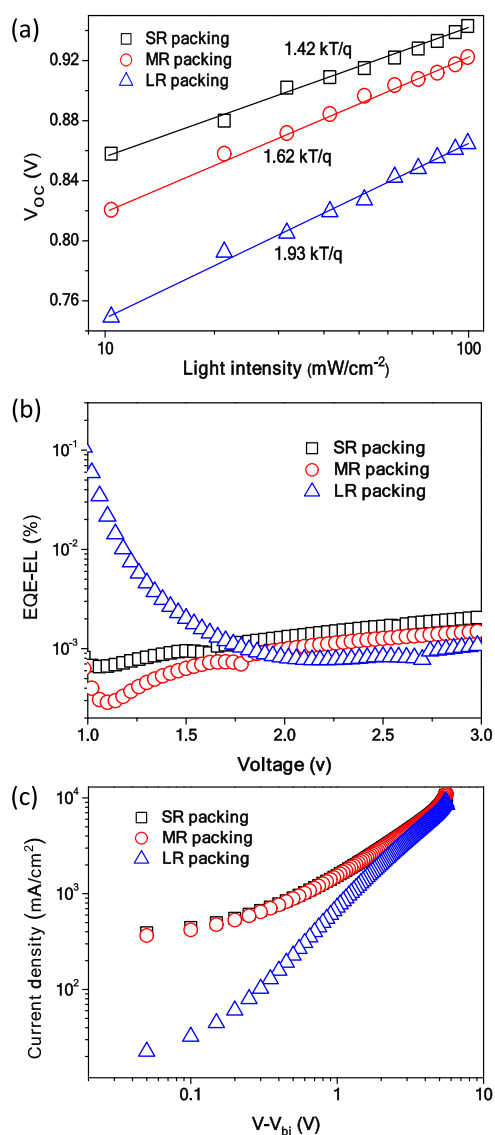


Figure 4. (a) Dependence of V_{oc} on light intensity and (b) electroluminescence quantum efficiency (EQE-EL) of bilayer devices with different PM7 molecular packing; (c) current density–applied voltage curves of PM7 devices with different molecular packing.

well-known, the slope of V_{oc} versus the natural logarithm of light intensity in the measurement gives kT/q , suggesting the dominated bimolecular recombination at open circuit. If the additionally trap-assisted charge recombination is involved, the slope will be greater than kT/q .^{42,43} Here, the fitted values of SR packing, MR packing, and LR packing devices are found to be 1.42, 1.62, and 1.93 kT/q , respectively. The gradually increasing slope in the LR packing device means that more trap-assisted charge recombination should be expected, which

is related closely with its morphological defects as discussed above. In addition, we also used other qualitative methods to confirm this claim. As shown in Figure 4b, electroluminescence quantum efficiency (EQE-EL) profiles of bilayer devices were studied. As analyzed by Nguyen et al.,⁴⁴ traps may induce the higher voltage-dependent EQE. We note that this also appears in the present LR packing device, while the other two devices display the relatively flat profiles. Interestingly, the current density–applied voltage curves of PM7 devices with different molecular packing show similar voltage dependence (Figure 4c). A typical trap-limited region emerges at the low-voltage range in the LR packing device,^{45,46} while the other two devices show similar shapes, in which the current density of the MR packing device is slightly lower than that of the SR packing device. We also calculated the corresponding hole mobility (μ_h) based on the current density–applied voltage curves. The values of μ_h for all the devices remain the same magnitude, while the specific numbers decreased from 3.01×10^{-5} to 2.91×10^{-5} and $2.39 \times 10^{-5} \text{ cm}^2 \text{ V}^{-1} \text{ s}^{-1}$ in the SR packing, MR packing, and LR packing devices, respectively. The electron mobility (μ_e) of the N2200 layer was examined as well, which is shown in Figure S13. The value was calculated to be $1.05 \times 10^{-4} \text{ cm}^2 \text{ V}^{-1} \text{ s}^{-1}$, which is greater than that of its PM7 counterparts.

Based on the analysis above, a clear landscape revealing the relationship between the morphological/energetic order and the photocurrent generation process has been constructed. The geometry of the PM7 molecular packing in the bilayer devices definitely and exclusively influences the energetic disorder at the D/A interface and the charge recombination dynamics. The extended CL of both face-on and edge-on crystals upon TA in PM7 films probably creates plenty of traps, which result from the reduced fraction of amorphous domains and expanding crystal boundaries. Those morphological defects should outcompete the driving force provided by the energetic offset in LR packing device and thereby inhibit the photocurrent generation process. Having established those crucial links, we try to explain the device parameter variations in the more complicated BHJ devices. Solvents with different boiling point, chloroform (CF) and o-dichlorobenzene (oDCB), were used to prepare the BHJ devices. As shown in Figure S14, the surface morphologies of CF and oDCB BHJ films were very similar, while the PM7 CL value of the oDCB film was larger than that of CF film as evidenced by the GIWAXS (Table S6). For the device performance, the J_{sc} values increased from 3.66 to 5.11 mA/cm² by using CF as processing solvent instead of oDCB, while the V_{oc} values improved from 0.93 to 1.00 V as well (Table S7). The light intensity-dependent V_{oc} profiles also suggest more trap-assisted charge recombination in the oDCB device. Therefore, we can discretely conclude that the increased PM7 molecular order is one possible, but not the exclusive, reason for the inefficient photocurrent generation and large energy loss in the oDCB device.

In conclusion, we have revealed the driving force for the photocurrent generation process in the PM7/N2200 bilayer models with small energetic offset. The morphological defects raised by the extended molecular order are believed to play an essential role. Diminishing morphological defects can not only increase the energetic order at the D/A interfaces which facilitates charge separation but also suppress the trap-assisted charge recombination process. Both of them contribute to a better J_{sc} and V_{oc} in the SR packing device. Our results indicate

that energetic offset is not the key factor influencing charge separation, while modulation of molecular and energetic order should be substantially considered in order to simultaneously enhance the photocurrent generation and reduce energy loss. This provides opportunities to manufacture efficient OSCs in terms of molecular morphology optimization.

■ ASSOCIATED CONTENT

Supporting Information

The Supporting Information is available free of charge at <https://pubs.acs.org/doi/10.1021/acsenerylett.0c00029>.

Experimental Section; UPS, photoluminescence, EQE, GIWAXS, and EQE measurement data (PDF)

■ AUTHOR INFORMATION

Corresponding Author

Wei Ma – State Key Laboratory for Mechanical Behavior of Materials, Xi'an Jiaotong University, Xi'an 710049, P.R. China; orcid.org/0000-0002-7239-2010; Email: msewma@xjtu.edu.cn

Authors

Ke Zhou – State Key Laboratory for Mechanical Behavior of Materials, Xi'an Jiaotong University, Xi'an 710049, P.R. China

Yanfeng Liu – Biomolecular and Organic Electronics, IFM, Linköping University, SE-581 83 Linköping, Sweden

Awad Alotaibi – Department of Physics and Astronomy, Washington State University, Pullman, Washington 99164, United States

Jian Yuan – State Key Laboratory for Mechanical Behavior of Materials, Xi'an Jiaotong University, Xi'an 710049, P.R. China

Chuanxiu Jiang – Division of Nanophotonics, CAS Key Laboratory of Standardization and Measurement for Nanotechnology, CAS Center for Excellence in Nanoscience, National Center for Nanoscience and Technology, Beijing 100191, P.R. China

Jingming Xin – State Key Laboratory for Mechanical Behavior of Materials, Xi'an Jiaotong University, Xi'an 710049, P.R. China

Xinfeng Liu – Division of Nanophotonics, CAS Key Laboratory of Standardization and Measurement for Nanotechnology, CAS Center for Excellence in Nanoscience, National Center for Nanoscience and Technology, Beijing 100191, P.R. China; orcid.org/0000-0002-7662-7171

Brian A. Collins – Department of Physics and Astronomy, Washington State University, Pullman, Washington 99164, United States; orcid.org/0000-0003-2047-8418

Fengling Zhang – Biomolecular and Organic Electronics, IFM, Linköping University, SE-581 83 Linköping, Sweden; orcid.org/0000-0002-1717-6307

Complete contact information is available at: <https://pubs.acs.org/doi/10.1021/acsenerylett.0c00029>

Notes

The authors declare no competing financial interest.

■ ACKNOWLEDGMENTS

The authors thank the Ministry of Science and Technology (No. 2016YFA0200700), NSFC (21704082, 21875182), China Postdoctoral Science Foundation (2017M623162), and 111 project 2.0 (BP2018008) for support. The authors thank Prof. Xiaofeng Xu at Ocean University of China for assistance with data acquisition. X-ray data were acquired at beamlines 7.3.3 at the Advanced Light Source, which is supported by the Director, Office of Science, Office of Basic

Energy Sciences, of the U.S. Department of Energy under Contract No. DE-AC02-05CH11231. The authors thank Chenhui Zhu at beamline 7.3.3 for assistance with data acquisition.

REFERENCES

- (1) Yuan, J.; Zhang, Y. Q.; Zhou, L. Y.; Zhang, G. C.; Yip, H. L.; Lau, T. K.; Lu, X. H.; Zhu, C.; Peng, H. J.; Johnson, P. A.; Leclerc, M.; Cao, Y.; Ulanski, J.; Li, Y. F.; Zou, Y. P. Single-Junction Organic Solar Cell with over 15% Efficiency Using Fused-Ring Acceptor with Electron-Deficient Core. *Joule* **2019**, *3*, 1140–1151.
- (2) Jiang, K.; Wei, Q.; Lai, J. L. Y.; Peng, Z.; Kim, H. K.; Yuan, J.; Ye, L.; Ade, H.; Zou, Y.; Yan, H. Alkyl Chain Tuning of Small Molecule Acceptors for Efficient Organic Solar Cells. *Joule* **2019**, *3*, 3020.
- (3) Meng, L.; Zhang, Y.; Wan, X.; Li, C.; Zhang, X.; Wang, Y.; Ke, X.; Xiao, Z.; Ding, L.; Xia, R.; Yip, H. L.; Cao, Y.; Chen, Y. Organic and Solution-Processed Tandem Solar Cells with 17.3% Efficiency. *Science* **2018**, *361*, 1094–1098.
- (4) Fan, Q. P.; Wang, Y.; Zhang, M. J.; Wu, B.; Guo, X.; Jiang, Y. F.; Li, W. B.; Guo, B.; Ye, C. N.; Su, W. Y.; Fang, J.; Ou, X. M.; Liu, F.; Wei, Z. X.; Sum, T. C.; Russell, T. P.; Li, Y. F. High-Performance As-Cast Nonfullerene Polymer Solar Cells with Thicker Active Layer and Large Area Exceeding 11% Power Conversion Efficiency. *Adv. Mater.* **2018**, *30*, 1704546.
- (5) Wang, G.; Adil, M. A.; Zhang, J.; Wei, Z. X. Large-Area Organic Solar Cells: Material Requirements, Modular Designs, and Printing Methods. *Adv. Mater.* **2019**, *31*, 1805089.
- (6) Traverse, C. J.; Pandey, R.; Barr, M. C.; Lunt, R. R. Emergence of Highly Transparent Photovoltaics for Distributed Applications. *Nat. Energy* **2017**, *2*, 849–860.
- (7) Cui, Y.; Wang, Y. M.; Bergqvist, J.; Yao, H. F.; Xu, Y.; Gao, B. W.; Yang, C. Y.; Zhang, S. Q.; Ingnas, O.; Gao, F.; Hou, J. H. Wide-gap Non-fullerene Acceptor Enabling High-Performance Organic Photovoltaic cells for Indoor Applications. *Nat. Energy* **2019**, *4*, 768–775.
- (8) Zhou, K.; Xin, J. M.; Ma, W. Hierarchical Morphology Stability under Multiple Stresses in Organic Solar Cells. *ACS Energy Lett.* **2019**, *4*, 447–455.
- (9) Mateker, W. R.; McGehee, M. D. Progress in Understanding Degradation Mechanisms and Improving Stability in Organic Photovoltaics. *Adv. Mater.* **2017**, *29*, 1603940.
- (10) Zhou, K.; Zhou, X.; Xu, X.; Musumeci, C.; Wang, C.; Xu, W.; Meng, X.; Ma, W.; Ingnas, O. π - π Stacking Distance and Phase Separation Controlled Efficiency in Stable All-Polymer Solar Cells. *Polymers* **2019**, *11*, 1665.
- (11) Hou, J. H.; Ingnas, O.; Friend, R. H.; Gao, F. Organic Solar Cells based on Non-Fullerene Acceptors. *Nat. Mater.* **2018**, *17*, 119–128.
- (12) Zhou, K.; Wu, Y.; Liu, Y. F.; Zhou, X. B.; Zhang, L.; Ma, W. Molecular Orientation of Polymer Acceptor Dominates Open-Circuit Voltage Losses in All-Polymer Solar Cells. *ACS Energy Lett.* **2019**, *4*, 1057–1064.
- (13) Benduhn, J.; Tvingstedt, K.; Piersimoni, F.; Ullbrich, S.; Fan, Y. L.; Tropiano, M.; McGarry, K. A.; Zeika, O.; Riede, M. K.; Douglas, C. J.; Barlow, S.; Marder, S. R.; Neher, D.; Spoltore, D.; Vandewal, K. Intrinsic Non-Radiative Voltage Losses in Fullerene-based Organic Solar Cells. *Nat. Energy* **2017**, *2*, 17053.
- (14) Vandewal, K.; Tvingstedt, K.; Gadisa, A.; Ingnas, O.; Manca, J. V. Relating the Open-Circuit Voltage to Interface Molecular Properties of Donor:Acceptor Bulk Heterojunction Solar Cells. *Phys. Rev. B: Condens. Matter Mater. Phys.* **2010**, *81*, 125204.
- (15) Vandewal, K.; Tvingstedt, K.; Manca, J. V.; Ingnas, O. Charge-Transfer States and Upper Limit of the Open-Circuit Voltage in Polymer: Fullerene Organic Solar Cells. *IEEE J. Sel. Top. Quantum Electron.* **2010**, *16*, 1676–1684.
- (16) Menke, S. M.; Ran, N. A.; Bazan, G. C.; Friend, R. H. Understanding Energy Loss in Organic Solar Cells: Toward a New Efficiency Regime. *Joule* **2018**, *2*, 25–35.
- (17) Nakano, K.; Chen, Y. J.; Xiao, B.; Han, W. N.; Huang, J. M.; Yoshida, H.; Zhou, E. J.; Tajima, K. Anatomy of the Energetic Driving Force for Charge Generation in Organic Solar Cells. *Nat. Commun.* **2019**, *10*, 2520.
- (18) Dimitrov, S. D.; Azzouzi, M.; Wu, J.; Yao, J.; Dong, Y.; Tuladhar, P. S.; Schroeder, B. C.; Bittner, E. R.; McCulloch, I.; Nelson, J.; Durrant, J. R. Spectroscopic Investigation of the Effect of Microstructure and Energetic Offset on the Nature of Interfacial Charge Transfer States in Polymer: Fullerene Blends. *J. Am. Chem. Soc.* **2019**, *141*, 4634–4643.
- (19) Qian, D. P.; Zheng, Z. L.; Yao, H. F.; Tress, W.; Hopper, T. R.; Chen, S. L.; Li, S. S.; Liu, J.; Chen, S. S.; Zhang, J. B.; Liu, X. K.; Gao, B. W.; Ouyang, L. Q.; Jin, Y. Z.; Pozina, G.; Buyanova, I. A.; Chen, W. M.; Ingnas, O.; Coropceanu, V.; Bredas, J. L.; Yan, H.; Hou, J. H.; Zhang, F. L.; Bakulin, A. A.; Gao, F. Design Rules for Minimizing Voltage Losses in High-Efficiency Organic Solar Cells. *Nat. Mater.* **2018**, *17*, 703–709.
- (20) Chen, S. S.; Wang, Y. M.; Zhang, L.; Zhao, J. B.; Chen, Y. Z.; Zhu, D. L.; Yao, H. T.; Zhang, G. Y.; Ma, W.; Friend, R. H.; Chow, P. C. Y.; Gao, F.; Yan, H. Efficient Nonfullerene Organic Solar Cells with Small Driving Forces for Both Hole and Electron Transfer. *Adv. Mater.* **2018**, *30*, 1804215.
- (21) Yao, H. F.; Cui, Y.; Qian, D. P.; Ponceca, C. S.; Honarfar, A.; Xu, Y.; Xin, J. M.; Chen, Z. Y.; Hong, L.; Gao, B. W.; Yu, R. N.; Zu, Y. F.; Ma, W.; Chabera, P.; Pullerits, T.; Yartsev, A.; Gao, F.; Hou, J. H. 14.7% Efficiency Organic Photovoltaic Cells Enabled by Active Materials with a Large Electrostatic Potential Difference. *J. Am. Chem. Soc.* **2019**, *141*, 7743–7750.
- (22) Yao, H. F.; Qian, D. P.; Zhang, H.; Qin, Y. P.; Xu, B. W.; Cui, Y.; Yu, R. N.; Gao, F.; Hou, J. H. Critical Role of Molecular Electrostatic Potential on Charge Generation in Organic Solar Cells. *Chin. J. Chem.* **2018**, *36*, 491–494.
- (23) Menke, S. M.; Cheminal, A.; Conaghan, P.; Ran, N. A.; Greeham, N. C.; Bazan, G. C.; Nguyen, T. Q.; Rao, A.; Friend, R. H. Order Enables Efficient Electron-Hole Separation at an Organic Heterojunction with a Small Energy Loss. *Nat. Commun.* **2018**, *9*, 277.
- (24) Graham, K. R.; Ndjawa, G. O. N.; Conron, S. M.; Munir, R.; Vandewal, K.; Chen, J. J.; Sweetnam, S.; Thompson, M. E.; Salleo, A.; McGehee, M. D.; Amassian, A. The Roles of Structural Order and Intermolecular Interactions in Determining Ionization Energies and Charge-Transfer State Energies in Organic Semiconductors. *Adv. Energy Mater.* **2016**, *6*, 1601211.
- (25) van Franeker, J. J.; Turbiez, M.; Li, W. W.; Wienk, M. M.; Janssen, R. A. J. A Real-Time Study of the Benefits of Co-Solvents in Polymer Solar Cell Processing. *Nat. Commun.* **2015**, *6*, 6229.
- (26) Lee, C.; Lee, S.; Kim, G. U.; Lee, W.; Kim, B. J. Recent Advances, Design Guidelines, and Prospects of All-Polymer Solar Cells. *Chem. Rev.* **2019**, *119*, 8028–8086.
- (27) Qian, D. P.; Liu, B.; Wang, S. H.; Himmelberger, S.; Linares, M.; Vagin, M.; Muller, C.; Ma, Z. F.; Fabiano, S.; Berggren, M.; Salleo, A.; Ingnas, O.; Zou, Y. P.; Zhang, F. L. Modulating Molecular Aggregation by Facile Heteroatom Substitution of Diketopyrrolopyrrole based Small Molecules for Efficient Organic Solar Cells. *J. Mater. Chem. A* **2015**, *3*, 24349–24357.
- (28) Liu, J.; Chen, S. S.; Qian, D. P.; Gautam, B.; Yang, G. F.; Zhao, J. B.; Bergqvist, J.; Zhang, F. L.; Ma, W.; Ade, H.; Ingnas, O.; Gundogdu, K.; Gao, F.; Yan, H. Fast Charge Separation in a Non-Fullerene Organic Solar Cell with a Small Driving Force. *Nat. Energy* **2016**, *1*, 16089.
- (29) Mai, J. Q.; Xiao, Y. Q.; Zhou, G. D.; Wang, J. Y.; Zhu, J. S.; Zhao, N.; Zhan, X. W.; Lu, X. H. Hidden Structure Ordering Along Backbone of Fused-Ring Electron Acceptors Enhanced by Ternary Bulk Heterojunction. *Adv. Mater.* **2018**, *30*, 1802888.
- (30) Ma, W.; Tumbleston, J. R.; Wang, M.; Gann, E.; Huang, F.; Ade, H. Domain Purity, Miscibility, and Molecular Orientation at Donor/Acceptor Interfaces in High Performance Organic Solar Cells: Paths to Further Improvement. *Adv. Energy Mater.* **2013**, *3*, 864–872.

(31) Yang, H. R.; Lai, Y. Y.; Lee, J. J. Further Examination of Interconnection in Conjugated Polymers for Organic Field-Effect Transistors. *Adv. Electron Mater.* **2019**, *5*, 1900213.

(32) Kastner, C.; Vandewal, K.; Egbe, D. A. M.; Hoppe, H. Revelation of Interfacial Energetics in Organic Multiheterojunctions. *Adv. Sci.* **2017**, *4*, 1600331.

(33) Clarke, T. M.; Durrant, J. R. Charge Photogeneration in Organic Solar Cells. *Chem. Rev.* **2010**, *110*, 6736–6767.

(34) Ran, N. A.; Roland, S.; Love, J. A.; Savikhin, V.; Takacs, C. J.; Fu, Y. T.; Li, H.; Coropceanu, V.; Liu, X. F.; Bredas, J. L.; Bazan, G. C.; Toney, M. F.; Neher, D.; Nguyen, T. Q. Impact of Interfacial Molecular Orientation on Radiative Recombination and Charge Generation Efficiency. *Nat. Commun.* **2017**, *8*, 79.

(35) Grancini, G.; Maiuri, M.; Fazzi, D.; Petrozza, A.; Egelhaaf, H. J.; Brida, D.; Cerullo, G.; Lanzani, G. Hot Exciton Dissociation in Polymer Solar Cells. *Nat. Mater.* **2013**, *12*, 29–33.

(36) Baran, D.; Gasparini, N.; Wadsworth, A.; Tan, C. H.; Wehbe, N.; Song, X.; Hamid, Z.; Zhang, W. M.; Neophytou, M.; Kirchartz, T.; Brabec, C. J.; Durrant, J. R.; McCulloch, I. Robust Nonfullerene Solar Cells Approaching Unity External Quantum Efficiency Enabled by Suppression of Geminate Recombination. *Nat. Commun.* **2018**, *9*, 2059.

(37) Ferron, T.; Waldrip, M.; Pope, M.; Collins, B. A. Increased Charge Transfer State Separation via Reduced Mixed Phase Interface in Polymer Solar Cells. *J. Mater. Chem. A* **2019**, *7*, 4536–4548.

(38) Kniepert, J.; Lange, I.; van der Kaap, N. J.; Koster, L. J. A.; Neher, D. A Conclusive View on Charge Generation, Recombination, and Extraction in As-Prepared and Annealed P3HT:PCBM Blends: Combined Experimental and Simulation Work. *Adv. Energy Mater.* **2014**, *4*, 1301401.

(39) Mandoc, M. M.; Veurman, W.; Koster, L. J. A.; de Boer, B.; Blom, P. W. M. Origin of the Reduced Fill Factor and Photocurrent in MDMO-PPV: PCNEPV All-Polymer Solar Cells. *Adv. Funct. Mater.* **2007**, *17*, 2167–2173.

(40) Gong, W.; Faist, M. A.; Ekins-Daukes, N. J.; Xu, Z.; Bradley, D. D. C.; Nelson, J.; Kirchartz, T. Influence of Energetic Disorder on Electroluminescence Emission in Polymer:Fullerene Solar Cells. *Phys. Rev. B: Condens. Matter Mater. Phys.* **2012**, *86*, 024201.

(41) Ran, N. A.; Love, J. A.; Takacs, C. J.; Sadhanala, A.; Beavers, J. K.; Collins, S. D.; Huang, Y.; Wang, M.; Friend, R. H.; Bazan, G. C.; Nguyen, T. Q. Harvesting the Full Potential of Photons with Organic Solar Cells. *Adv. Mater.* **2016**, *28*, 1482–1488.

(42) Kyaw, A. K. K.; Wang, D. H.; Gupta, V.; Leong, W. L.; Ke, L.; Bazan, G. C.; Heeger, A. J. Intensity Dependence of Current-Voltage Characteristics and Recombination in High-Efficiency Solution-Processed Small-Molecule Solar Cells. *ACS Nano* **2013**, *7*, 4569–4577.

(43) Nian, L.; Kan, Y. Y.; Wang, H. T.; Gao, K.; Xu, B.; Rong, Q. K.; Wang, R.; Wang, J.; Liu, F.; Chen, J. W.; Zhou, G. F.; Russell, T. P.; Jen, A. K. Y. Ternary Non-Fullerene Polymer Solar Cells with 13.51% Efficiency and a Record-High Fill Factor of 78.13%. *Energy Environ. Sci.* **2018**, *11*, 3392–3399.

(44) Rosenthal, K. D.; Hughes, M. P.; Luginbuhl, B. R.; Ran, N. A.; Karki, A.; Ko, S. J.; Hu, H.; Wang, M.; Ade, H.; Nguyen, T. Q. Quantifying and Understanding Voltage Losses Due to Nonradiative Recombination in Bulk Heterojunction Organic Solar Cells with Low Energetic Offsets. *Adv. Energy Mater.* **2019**, *9*, 1901077.

(45) Nikolka, M.; Broch, K.; Armitage, J.; Hanifi, D.; Nowack, P. J.; Venkateshvaran, D.; Sadhanala, A.; Saska, J.; Mascal, M.; Jung, S. H.; Lee, J. K.; McCulloch, I.; Salleo, A.; Sirringhaus, H. High-Mobility, Trap-Free Charge Transport in Conjugated Polymer Diodes. *Nat. Commun.* **2019**, *10*, 2122.

(46) Kotadiya, N. B.; Mondal, A.; Blom, P.; Andrienko, D.; Wetzelaer, G. A. H. A Window to Trap-Free Charge Transport in Organic Semiconducting Thin Films. *Nat. Mater.* **2019**, *18*, 1182–1186.